Joshua D. Bocarsly, ^{1,*} M.D. Johannes, ² Stephen D. Wilson, ¹ and Ram Seshadri ¹ Materials Department and Materials Research Laboratory, University of California, Santa Barbara, California 93106, United States ² Center for Computational Materials Science, Naval Research Laboratory

Washington, D.C. 20375, United States (Dated: October 13, 2020)

An understanding of the origins of giant magnetostructural coupling is developed for the compound MnAs, a magnetic material that has served as a prototype for many promising technologies including caloric refrigeration, magnetic actuation, and spintronics. We demonstrate that strong coupling between magnetism and crystal structure arises from an orbital-specific competition between exchange energies and kinetic (bonding) energies and that thermally activated spin-fluctuations drive the unusual first-order phase transition from high to low symmetry upon heating. The underlying mechanism raises the prospect of an exotic paramagnetic state featuring local fluctuations in atomic positions and bonding on the time scale of the moment fluctuations. The results should inform the design of new materials with enhanced magnetostructural coupling, found at the border between structural and magnetic stability.

Since the 1950s [1–6], MnAs has served as the prototypical material for strong coupling between magnetism and crystal structure. Upon heating, a dramatic firstorder magnetostructural phase transition is observed at $T_C = 318 \,\mathrm{K}$, whereupon the ferromagnetic (FM) hexagonal structure transforms to a lower-symmetry paramagnetic (PM) orthorhombic structure with a 2.5% smaller unit cell volume. As the temperature is further increased, the hexagonal structure is recovered via a continuous transition around $T_t = 398 \,\mathrm{K}$. The transition at T_C is of great interest because it can be actuated by temperature, field, and mechanical stress. In particular, a moderate magnetic field can be used to drive giant entropy changes in MnAs, enabling magnetic refrigeration based on the magnetocaloric effect [7–9]. Other promising magnetocalorics, such as $Gd_5(Si,Ge)_4$, MnFe(P,X), and doped LaMnO₃ display similarly strong coupling [10–16]; however, the microscopic mechanism governing giant magnetostructural coupling in MnAs and related materials remains an open question.

In the ground state structure of MnAs, Mn is arranged on a hexagonal lattice [Fig. 1(a)], with large spacing (3.72 Å) within the basal plane and short spacing (2.85 Å) perpendicular to the plane. Upon heating above 318 K or applying pressures above 2 kbar [17], first-order transitions to orthorhombic symmetry are observed [Fig. 1(b)]. In these transitions, alternating rows of Mn move towards each other within the plane to create Mn-Mn zigzag chains with shorter contacts lengths (3.38 Å at ambient pressure), while alternating rows of As atoms move a similar distance in the perpendicular direction. We refer to the magnitudes of these modes within the orthorhombic cell as $\delta_{\rm Mn} = \Delta \, {\rm Mn}_z/c$ and $\delta_{\rm As} = \Delta {\rm As}_x/a$, indicating deviations of the atoms' fractional coordinates from their ideal hexagonal positions. At 318 K and ambient pressure, $\delta_{\rm Mn}$ and $\delta_{\rm As}$ are 0.027 and 0.025, respectively [18].

There have been numerous attempts to explain the

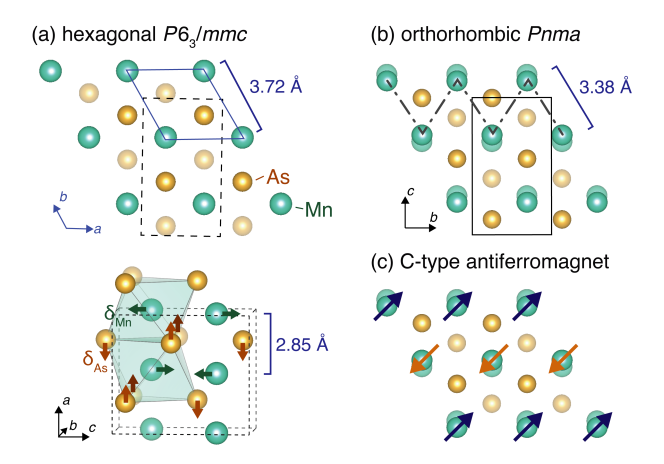


FIG. 1. Structure of MnAs in its (a) hexagonal and (b) orthorhombic forms. In (a), the orthohexagonal cell is shown in dashed lines and, at the bottom, the arrows indicate the directions of the atomic displacements that give rise to the orthorhombic structure. (c) The previously proposed C-type antiferromagnetic structure of the orthorhombic phase. All correlations out of the shown plane are ferromagnetic.

behavior of MnAs [4–6, 19–22]. Goodenough and coworkers proposed that the transitions are Mn³⁺ high-spin to low-spin transformations [6, 17, 23]. Conversely, Bean and Rodbell proposed a phenomenological model where a first-order transition can be realized in a sufficiently compressible material with a strongly volume-dependent magnetic exchange [4, 5]. More recent computational efforts have concluded that the orthorhombic structure above T_C is actually antiferromangetic (AFM), with the Mn moments alternating direction along the zigzag chains [C-type AFM, Fig. 1(c)] [19, 24–26]. However, neutron diffraction points to a PM state without long-range order [3], and paramagnetic scattering experiments [27, 28] and chemical substitution studies [29] indicate ferromagnetic correlations and a local moment magnitude that remains

approximately constant across T_C . Furthermore, a variety of unusual physical properties reported in MnAs are largely unexplained, including the large amounts of local atomic disorder [30, 31], anomalous elastic properties [32, 33], and extremely low thermal conductivity [34]. Microscopic understanding consistent with the experimental situation has, so far, clearly been missing.

Here, we use electronic structure calculations on ordered and disordered magnetic states to establish physical mechanisms for both the pressure-driven and temperature-driven phase transitions in MnAs. Both transitions are found to arise from orbital-specific competition between kinetic energy and different types of exchange energies: intra-atomic Hund's coupling for the pressure-driven transition, and interatomic magnetic exchange for the temperature-driven transition. Furthermore, our calculations suggest that this competition may become dynamic in the paramagnetic phase as magnetic fluctuations couple with large fluctuations in interatomic spacing. This is expected to result in an unusual disordered phase, which can explain the anomalous elastic and transport behavior.

We began our investigation by performing density functional theory-based calculations (DFT) [35–37] on MnAs using a generalized gradient approximation (PBEsol [39]). Starting with the experimental ambient pressure hexagonal [40] and orthorhombic [18] structures and ferromagnetic moments, we fully relaxed the lattice parameters and internal atomic coordinates. This resulted in cells with volumes respectively 13% and 19% smaller than experiment, in contrast with the typical slight overestimation of volumes often associated with the PBEsol approximation [41]. Additionally, the DFT energy of the orthorhombic cell was found to be lower than that of the hexagonal cell by 181 meV f.u.⁻¹, a result that is clearly unphysical given that the experimental ground state is ferromagnetic and hexagonal. Previous DFT studies have not addressed this inconsistency [25, 42], presumably because a full relaxation into the global orthorhombic minimum was not investigated.

Employing the DFT+U electron correlation correction via Dudarev's $U - J = U_{\text{eff}}$ formalism [43] localizes the Mn d states that are systematically too diffuse in standard DFT [44] and brings both the lattice parameters and magnetic moments (3.4 μ_B per Mn) of the hexagonal cell into good agreement with experiment for $U_{\text{eff}} = 1.2 \text{ eV}$ with the PBEsol functional [Fig. S1,S2]. Perhaps more importantly, this $U_{\rm eff}$ proves to be the critical variable to correct the energetics, and the hexagonal cell is now 92 meV f.u.⁻¹ lower in energy than the orthorhombic one. We also tried calculations with the standard PBE functional, and found very similar results: without U, the volumes are underestimated and the ground state is incorrect. The energetics and volume, however, can be corrected with a small $U_{\text{eff}} = 0.5 \,\text{eV}$, which gives similar results to PBEsol with $U_{\text{eff}} = 1.2 \,\text{eV}$ [Fig. S3].

Proceeding with PBEsol and $U_{\text{eff}} = 1.2 \,\text{eV}$, we found

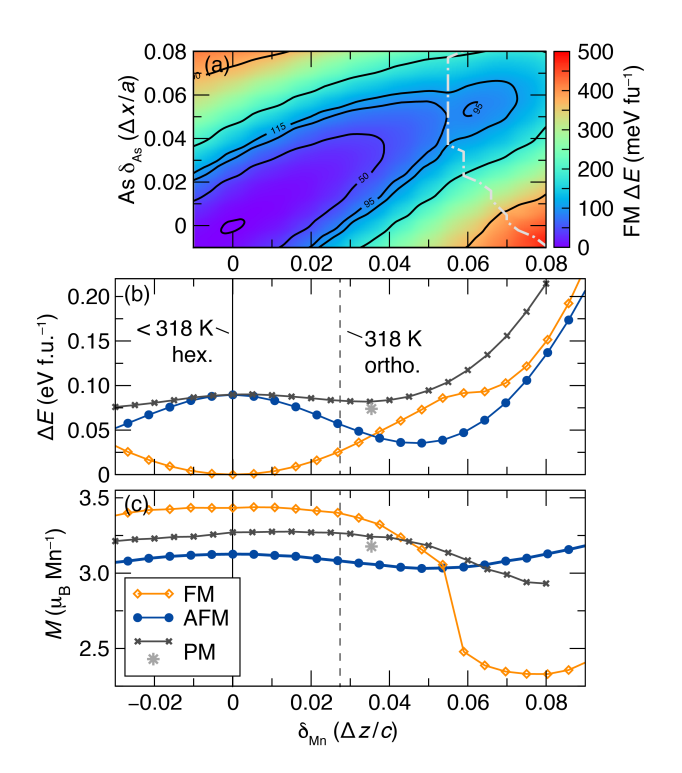


FIG. 2. (a) 2D energy surface of ferromagnetic MnAs as a function of Mn distortion and As distortion. (b) 1D energy surfaces of ferromagnetic (FM), antiferromagnetic (AFM), and paramagnetic (PM) MnAs as a function of Mn distortion. (c) Corresponding Mn local moment magnitudes.

that the metastable orthorhombic state has a smaller Mn moment than the hexagonal ground state $(2.4\,\mu_B)$ vs. $3.4\,\mu_B$). This moment and the DFT lattice parameters closely match (within 2%) the experimental state obtained at low temperatures by applying pressure [45]. This indicates that the pressure-driven transition is consistent with a high-moment to low-moment transition. However, the volume of this orthorhombic cell is still 16% smaller than the ambient pressure orthorhombic cell observed at 318 K, and the $\delta_{\rm Mn}$ is much larger (0.061 vs. 0.027); therefore this low-moment cell can only explain the pressure-driven transition, not the thermally-driven transition.

We further investigated the energy surface of ferromagnetic MnAs during its transition from high-moment hexagonal to low-moment orthorhombic as a function of $\delta_{\rm Mn}$ and $\delta_{\rm As}$. Figure 2(a) shows a 2D energy surface created from 900 calculations where Mn z and As x positions were held fixed, while all other coordinates and the lattice parameters were allowed to freely relax. We obtain a double-welled energy surface with local minima at the hexagonal structure ($\delta_{\rm Mn}=0$, $\delta_{\rm As}=0$) and in the low-moment orthorhombic structure ($\delta_{\rm Mn}=0.061$, $\delta_{\rm As}=0.053$), with the barrier between these wells indicated with a white dashed line running principally vertically on the phase diagram. This analysis shows that

the transition is driven by the Mn sublattice: moving the Mn atoms without movement of the As atoms can traverse the phase transition line, but not vice-versa. We therefore proceed to plot the 1D energy surface and local Mn moment as a function of $\delta_{\rm Mn}$ only [Fig. 2(b-c)], where the As x position is now allowed to freely relax along with the other structural parameters. Here, a sharp drop in moment from $3.4\,\mu_{\rm B}$ to $2.4\,\mu_{\rm B}$ is observed as the hexagonal-to-orthorhombic phase boundary is crossed.

When we instead impose the C-type AFM structure, the energy surface looks very different. The potential is now single-welled, with an energy maximum at $\delta_{\rm Mn} = 0$ and minimum at $\delta_{\rm Mn} = 0.05$. Additionally, the local moment is virtually independent of δ_{Mn} . The magnetic stabilization energy (FM minus AFM), which is proportional to Mn-Mn magnetic exchange energy along the zigzag chain, is at its most negative at $\delta_{\rm Mn} = 0$, and changes sign to positive (favoring AFM) for $\delta_{\rm Mn} > 0.035$, consistent with a previous extended Heisenberg model investigation [42]. Notably, the experimental ambient-pressure 318 K orthorhombic cell has $\delta_{\rm Mn} = 0.027$, and $\delta_{\rm Mn}$ decreases as temperature rises. [46] Therefore, ambient-pressure MnAs always falls within the regime where ferromagnetic exchange dominates ($\delta_{\rm Mn}$ < 0.035), corroborating the experimental observation that the paramagnetic correlations are ferromagnetic, not antiferromagnetic. [27, 28]

At ambient pressure and 318 K, the observed $\delta_{\rm Mn} = 0.027$ is close to the crossover in FM and AFM energies, consistent with the formation of a spin-fluctuationbased paramagnetic state. Since the dynamics of such a state are out of reach for DFT calculations, we simulate the paramagnetism using a special quasirandom structure (SQS) methodology [47], which has recently been applied successfully to paramagnets [48–51]. This approach involves constructing a supercell [we used the 96-atom supercell shown in Fig. 5(a)] and adjusting quasirandom up and down moments on the Mn atoms such that the local spin-spin correlations match the correlations of an infinite paramagnet (see Supplemental Material for details). When this disordered local moment cell is fully relaxed [gray star in Fig. 2(b-c)], it adopts an orthorhombic structure with the individual Mn and As atoms each relaxing differently in accordance with the broken local symmetries of the disordered cell. Overall, the average $\delta_{\rm Mn}$ is 0.035 \pm 0.006. Even though this SQS calculation represents a static model for a dynamic phenomenon (paramagnetism), the agreement with experiment is remarkably good: the fully-relaxed SQS cell has an average local magnetic moment of $3.2 \mu_B$ per Mn, comparing well with $3.1 \mu_B$ from paramagnetic neutron scattering [27]. The relaxed lattice parameters are also all within 3% of their experimental 318 K values [18] (Table S2).

Fig. 2(b-c) also shows an energy surface for the disordered state, calculated using a smaller 64-atom SQS by fixing the $\delta_{\rm Mn}$ values but allowing all other structural degrees of freedom to relax. This surface shows a very

shallow minimum around $\delta_{\rm Mn}=0.035$ and a maximum at $\delta_{\rm Mn}=0$. We note that, by construction, the SQS calculations give higher energies than the ordered states, as the entropy which stabilizes the paramagnet is not considered in the calculated energy.

From these calculations, we can see that it is the high-moment ferromagnetism that establishes the highsymmetry lattice: any pressure or temperature sufficient to disrupt this magnetic configuration towards PM, AFM, or low-moment FM states will simultaneously drive a structural distortion to orthorhombic. To understand the origins of this behavior, we investigated the orbital bonding properties of MnAs. While Mn sits in a nearly perfect octahedron in the hexagonal structure, we found that the expected octahedral crystal field splitting is absent from the electronic structure [Supplemental Material Fig. S5]. This indicates that direct Mn-Mn interactions beyond the immediate Mn-As coordination shell play a significant role in the electronic structure, reminiscent of the FeAs family of superconductors which also exhibit strong and unusual magnetostructural coupling [52, 53].

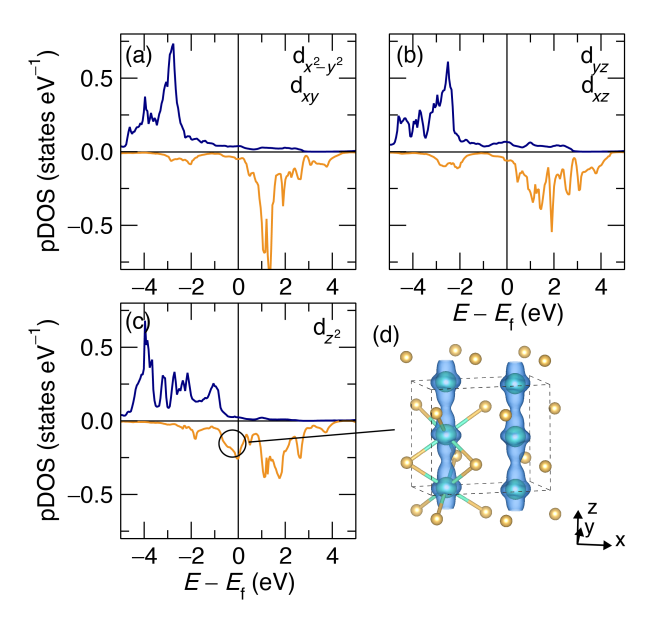


FIG. 3. (a-d) Projected Mn d-orbital partial densities of states for the ferromagnetic, hexagonal structure, using a projection scheme oriented around the Mn-Mn contacts. Majority spin states are shown as positive DOS values, and minority as negative. (a-b) $d_{x^2-y^2}$, d_{xy} , d_{yz} , and d_{xz} orbitals are all fully spin-polarized, stabilized by Hund's coupling. (c) The d_{z^2} orbital is more dispersive and is stabilized by Mn-Mn bonding, as shown in (d) the partial charge density of the minority spin channel within 1 eV below the fermi level.

We therefore reoriented the d orbital basis according to the Mn-Mn contacts, as illustrated in Figs. 3(d) and Fig. 4(a). In this scheme, the d_{z^2} orbital lobes point out of the plane, along the nearest-neighbor Mn-Mn contact, while one lobe of the $d_{x^2-y^2}$ orbital points along the Mn-Mn zigzag contact that is activated by the dis-

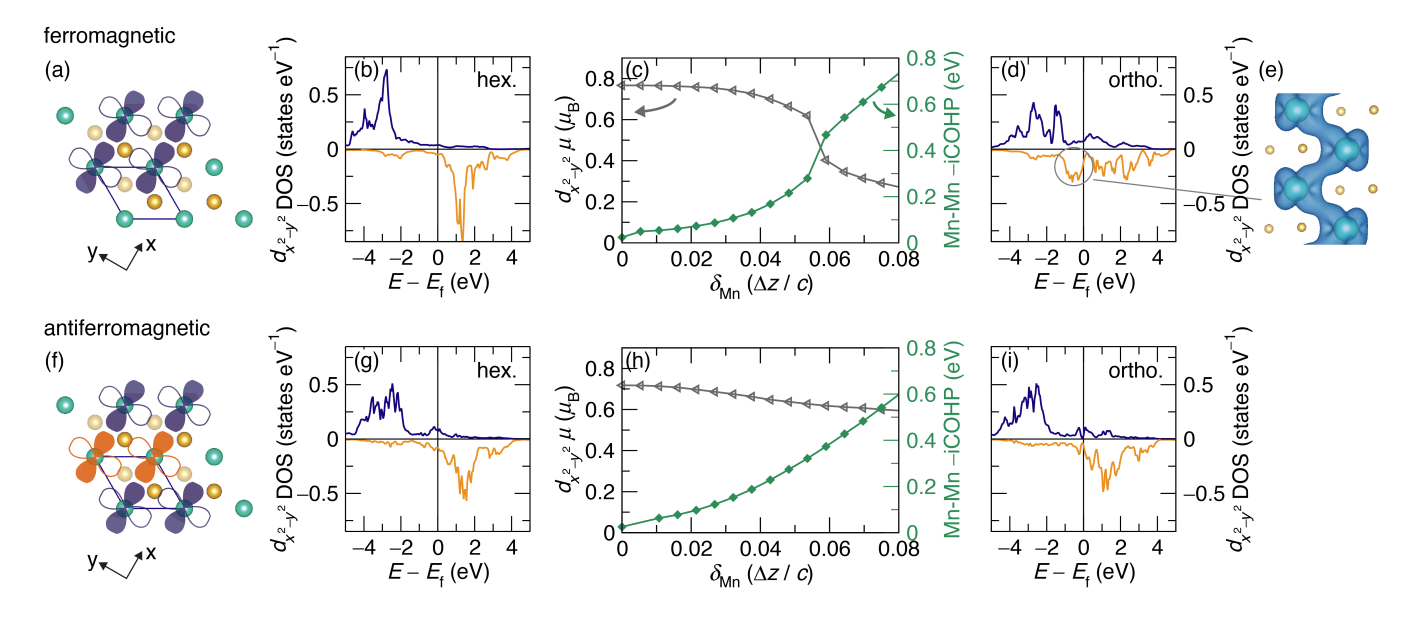


FIG. 4. Single-orbital properties of MnAs in the FM (a-e) and C-type AFM (f-i) structures. (a) Mn $d_{x^2-y^2}$ orbitals oriented along Mn-Mn contacts. (b,d) Projected partial $d_{x^2-y^2}$ DOS for the hexagonal and orthorhombic structures, respectively. (c) Projected $d_{x^2-y^2}$ moment and negative integrated crystal orbital Hamilton populations (-iCOHP) of the Mn-Mn zigzag contact as a function of Mn distortion. (e) Partial charge density of the minority spin channel within 1 eV below the fermi level for low-moment ferromagnetic, orthorhombic MnAs. (f-i) show the same data as (a-e), except for the AFM case.

tortion. In the hexagonal structure, $d_{x^2-y^2}$ and d_{xy} are degenerate, and d_{yz} and d_{xz} are degenerate. As shown in Fig. 3, all of the Mn d orbitals except d_{z^2} show partial DOS that are approximately half-filled with the majority spin states localized about 2.5 eV below the Fermi level with unoccupied minority spin states above. This electronic structure is stabilized by Hund's coupling (i.e. intra-atomic exchange), which is the driving force for the splitting of majority and minority spin states. Since only the majority spin states are occupied, this splitting lowers the energy. Conversely, the d_{z^2} orbital shows a much more dispersive DOS consistent with a band formed by Mn-Mn bonding along the short contacts Fig. 3(d). For this orbital, it is the kinetic energy benefit associated with chemical bonding that stabilizes the electronic structure.

In our projection scheme, the $d_{x^2-y^2}$ orbital shows large changes in projected moment when a Mn distortion is introduced (Fig. 4.), while the other d orbitals are comparatively unaffected (Fig. S6). In the ferromagnetic case, as the distortion forces Mn atoms together, overlap of the neighboring $d_{x^2-y^2}$ orbitals makes full spin-polarization untenable due to the Pauli exclusion principle, as electrons with the same spin cannot overlap spatially. This precipitates an electronic transition, seen in the reorganization of the DOS from a fully spin-polarized, localized structure in Fig. 4(b) to a much more dispersive structure in Fig. 4(d). The new electronic structure loses the Hund's coupling stabilization, but partially compensates by forming Mn-Mn bonds along the zigzag chain [Fig. 4(e)]. The competition between Hund's coupling and bonding is

clearly seen in Fig. 4(c), which shows the $d_{x^2-y^2}$ moment and the Mn-Mn zigzag contact bond strength (estimated using the integrated crystal orbital Hamilton population (-iCOHP) [54–58]) as a function of $\delta_{\rm Mn}$. As $\delta_{\rm Mn}$ increases, the moment drops precipitously, while the -iCOHP rises from 0 eV to 0.6 eV, indicating the formation of a Mn-Mn bond. Furthermore, the orthorhombic distortion also increases the Mn-As and As-As -iCOHPs [Fig. S7] as the asymmetric coordination optimizes bond distances. Altogether, these favorable bonding interactions explain the local stability of the low-moment orthorhombic state.

Therefore, we can see that the high-moment hexagonal to low-moment orthorhombic transition experienced by MnAs under pressure can be understood as arising from a competition between Hund's coupling and chemical bonding. At ambient pressure, the Hund's coupling stabilization outweighs the kinetic energy consideration. However, the application of pressure forces a reorganization of the electrons to comply with the Pauli principle, destabilizing the high-volume high-moment state in favor of a lower-moment, more strongly bonded structure.

Even though the AFM state is never observed experimentally, it is informative to consider its behavior in order to understand how spin flips modify the system [Fig 4(f-i)]. In the AFM case, the Mn atoms that are brought together by the distortion have opposite spins and the Pauli exclusion principle does not come into play. As the $d_{x^2-y^2}$ orbitals begin to overlap, they are able to hybridize and form a metal-metal bond without disrupting the spin polarization. For this reason, the Mn local

moment magnitudes remain approximately constant as a function of $\delta_{\rm Mn}$, and bonding and moment can all be simultaneously optimized at $\delta_{\rm Mn}=0.05$. However, this AFM state is not the ground state due to non-optimized inter-atomic magnetic exchange [i.e. FM – AFM energy in Fig. 2(b)]. As discussed previously, this exchange is optimized at $\delta_{\rm Mn}=0$, stabilizing the FM hexagonal ground state.

Based on the analysis of the FM, AFM and SQS states, we are now equipped to understand why the ambientpressure transition from ferromagnetic to paramagnetic is coupled to a large structural distortion. The hexagonal ground state is not optimized from a bonding perspective, but maximizes both interatomic magnetic exchange energy and Hund's coupling and is therefore lower in energy than all competing states. As temperature rises and spin-flip fluctuations begin to set in, the magnetic exchange energy benefit is weakened, and, at 318 K, it becomes more favorable to structurally distort, forgoing the interatomic exchange energy in favor of the kinetic energy (bonding) stabilization of the orthorhombic state. The spin fluctuations aid this transition by introducing AFM pairs of Mn atoms along the zigzag chains, allowing $d_{x^2-y^2}$ orbitals to partially maintain their Hund's coupling stabilization when distorting. Interestingly, all the competition takes place in the $d_{x^2-y^2}$ orbital channel. The small Mn-Mn contact length along the d_{z^2} orbital causes it to remain in the bonded state at all temperatures, while long Mn-Mn contacts along the other orbitals cause them to stay in their spin-polarized Hund's coupled states at all temperatures. Therefore, the key to this transition is the competition between exchange and bonding energies in half-filled Mn-Mn orbitals that are just on the verge of possible overlap.

This interplay between magnetic exchange, magnetic moment, and structural distortion has interesting implications for the paramagnetic state. In the fully-relaxed SQS cell, we observed that the Mn and As atoms relaxed away from their symmetrical sites by up to 0.2 Å, leading to very different local environments for different atoms. Such large local distortions have not been seen in other paramagnets simulated using the SQS method [48–51]. Figure 5(a) shows the relaxed SQS cell, and Fig. 5(b) shows all of the atoms from this supercell projected into a single primitive unit cell. Here, it can be seen that Mn and As atoms cluster into elongated clouds along the hexagonal-to-orthorhombic distortion modes; evidently, the PM state is most stable with a distribution of $\delta_{\rm Mn}$ and δ_{As} values. In fact, this unusual finding can be connected to the mechanism of magnetostructural coupling described above. Fig. 5 shows the Mn-Mn spacing (c) and bond strengths [-iCOHP, (d)] for each of the 48 Mn-Mn contacts along the zigzag chains in the SQS, plotted as a function of whether the pairs of atoms have the same spin direction or opposite spin direction. On average, the AFM pairs have bond distances 0.1 Å (3%) shorter

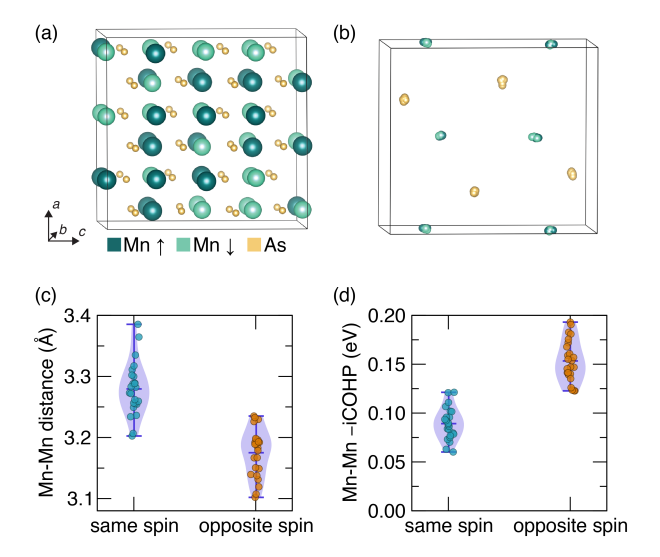


FIG. 5. (a) Structurally-relaxed SQS used to simulate the paramagnetic state. (b) Projection of the supercell atomic positions into a single orthorhombic cell, showing Mn and As occupying a distribution of positions along the structural distortion modes. (c) Distributions of bond distance and (d) negative integrated crystal orbital Hamilton population for the 48 unique Mn-Mn zigzag contacts.

than FM pairs, and bond strengths about twice as large. This is consistent with the idea that the Pauli exclusion principle disfavors $d_{x^2-y^2}$ orbital overlap in FM pairs of Mn atoms, but not in AFM pairs. Importantly, the other Mn-Mn contacts in the structure, along other d orbitals, show no dependence of the bond lengths or strengths on the spin correlation [Fig. S8], highlighting once again that the competition-driven coupling occurs selectively in the Mn $\mathrm{d}_{x^2-y^2}$ orbitals.

The dependence of Mn-Mn bonding on local spin configuration implies that in the paramagnetic state of MnAs, thermal spin fluctuations can be expected to couple to large atomic displacements accompanied by the dynamic formation and breaking of metal-metal bonds. We predict this exotic disordered state should be detectable by large and dynamic local-symmetry breaking [30, 31], as well as strong magneto-vibrational inelastic neutron scattering, and anomalous thermal and spin transport. In particular, the local atomic disorder caused by this state may be invoked to explain the extremely low thermal conductivity [34] and the abnormal elastic properties [32, 33]. Furthermore, the mechanisms for magnetostructural coupling driven by competition between exchange and kinetic energy scales described here are expected to be a general feature of other systems displaying strong coupling, and similar features of the disordered magnetic states may be expected.

This work was supported by the National Science Foundation through the DMR-1710638. Partial support to SDW through the NSF Materials Research Science and

Engineering Center (DMR-1720256, IRG-1) is acknowledged. MDJ acknowledges support from the Agile ICME Project from ONR, contract number N0001418RX00212. Computational facilities were supported through NSF CNS-1725797 and DMR-1720256 administered by the Center for Scientific Computing. JDB was supported by the NSF Graduate Research Fellowship Program under Grant No. DGE-1650114. We thank Professor Chris Van de Walle for helpful discussions.

- * jdbocarsly@mrl.ucsb.edu
- [1] C. Guillaud, J. Phys. le Radium 12, 223 (1951).
- [2] B. T. M. Willis and H. P. Rooksby, Proc. Phys. Soc. Sect. B 67, 290 (1954).
- [3] G. E. Bacon and R. Street, Nature 175, 518 (1955).
- [4] C. P. Bean and D. S. Rodbell, Phys. Rev. 126, 104 (1962).
- [5] R. W. De Blois and D. S. Rodbell, Phys. Rev. **130** (1963).
- [6] J. B. Goodenough and J. A. Kafalas, Phys. Rev. 157, 389 (1967).
- [7] H. Wada and Y. Tanabe, Appl. Phys. Lett. 79, 3302 (2001).
- [8] V. K. Pecharsky and K. A. Gschneidner, Jr., Phys. Rev. Lett. 78, 4494 (1997).
- [9] V. Franco, J. Blázquez, J. Ipus, J. Law, L. Moreno-Ramírez, and A. Conde, Prog. Mater. Sci. 93, 112 (2018).
- [10] W. Choe, V. K. Pecharsky, A. O. Pecharsky, K. A. Gschneidner, V. G. Young, and G. J. Miller, Phys. Rev. Lett. 84, 4617 (2000).
- [11] N. H. Dung, L. Zhang, Z. Q. Ou, and E. Brück, Appl. Phys. Lett. 99, 092511 (2011).
- [12] Z. B. Guo, Y. W. Du, J. S. Zhu, H. Huang, W. P. Ding, and D. Feng, Phys. Rev. Lett. 78, 1142 (1997).
- [13] M. E. Gruner, W. Keune, B. Roldan Cuenya, C. Weis, J. Landers, S. I. Makarov, D. Klar, M. Y. Hu, E. E. Alp, J. Zhao, M. Krautz, O. Gutfleisch, and H. Wende, Phys. Rev. Lett. 114, 057202 (2015).
- [14] A. Barcza, Z. Gercsi, K. S. Knight, and K. G. Sandeman, Phys. Rev. Lett. 104, 247202 (2010).
- [15] J. D. Bocarsly, E. E. Levin, C. A. C. Garcia, K. Schwennicke, S. D. Wilson, and R. Seshadri, Chem. Mater. 29, 1613 (2017).
- [16] J. D. Bocarsly, E. E. Levin, S. A. Humphrey, T. Faske, W. Donner, S. D. Wilson, and R. Seshadri, Chem. Mater. 31, 4873 (2019).
- [17] N. Menyuk, J. A. Kafalas, K. Dwight, and J. B. Goodenough, Phys. Rev. 177, 942 (1969).
- [18] R. H. Wilson and J. S. Kasper, Acta Crystallogr. 17, 95 (1964).
- [19] C. Kittel, Phys. Rev. 120, 335 (1960).
- [20] M. Shimizu, Proc. Phys. Soc. 84, 397 (1964).
- [21] S. K. Asadov, É. A. Zavadskii, V. I. Kamenev, E. P. Stefanovskii, A. L. Sukstanskii, and B. M. Todris, Phys. Solid State 42, 1696 (2000).
- [22] V. I. Val'kov and A. V. Golovchan, Low Temp. Phys. 30, 711 (2004).
- [23] J. Mira, F. Rivadulla, J. Rivas, A. Fondado, T. Guidi, R. Caciuffo, F. Carsughi, P. G. Radaelli, and J. B. Goodenough, Phys. Rev. Lett. 90, 097203 (2003).
- [24] M. K. Niranjan, B. R. Sahu, and L. Kleinman, Phys.

- Rev. B 70, 180406(R) (2004).
- [25] J. Lażewski, P. Piekarz, J. Toboła, B. Wiendlocha, P. T. Jochym, M. Sternik, and K. Parlinski, Phys. Rev. Lett. 104, 147205 (2010).
- [26] J. Lażewski, P. Piekarz, and K. Parlinski, Phys. Rev. B 83, 054108 (2011).
- [27] L. H. Schwartz, E. L. Hall, and G. P. Felcher, J. Appl. Phys. 42, 1621 (1971).
- [28] K. U. Neumann, K. R. Ziebeck, F. Jewiss, L. Däweritz, K. H. Ploog, and A. Murani, Phys. B Condens. Matter 335, 34 (2003).
- [29] K. Selte, A. Kjekshus, A. F. Andresen, and A. Zieba, J. Phys. Chem. Solids 38, 719 (1977).
- [30] G. A. Govor, Phys. status solidi 90, K185 (1985).
- [31] O. Palumbo, C. Castellano, A. Paolone, and R. Cantelli, J. Phys. Condens. Matter 17, 1537 (2005).
- [32] M. Dörfler and K. Bärner, Phys. Status Solidi 17, 141 (1973).
- [33] K. Bärner and H. Berg, Phys. Status Solidi 49, 545 (1978).
- [34] S. Fujieda, Y. Hasegawa, A. Fujita, and K. Fukamichi, J. Appl. Phys. 95, 2429 (2004).
- [35] G. Kresse and J. Furthmüller, Phys. Rev. B 54, 11169 (1996).
- [36] P. E. Blöchl, Phys. Rev. B **50**, 17953 (1994).
- [37] G. Kresse and D. Joubert, Phys. Rev. B 59, 1758 (1999).
- [38] J. P. Perdew, K. Burke, and M. Ernzerhof, Phys. Rev. Lett. 77, 3865 (1996).
- [39] J. P. Perdew, A. Ruzsinszky, G. I. Csonka, O. A. Vydrov, G. E. Scuseria, L. A. Constantin, X. Zhou, and K. Burke, Phys. Rev. Lett. 100, 136406 (2008).
- [40] A. Zieba, K. Selte, A. Kjekshus, A. F. Andresen, O. Smidsrød, C.-O. Pontchour, P. Phavanantha, S. Pramatus, B. N. Cyvin, and S. J. Cyvin, Acta Chem. Scand. 32a, 173 (1978).
- [41] P. Haas, F. Tran, and P. Blaha, Phys. Rev. B 79, 085104 (2009).
- [42] İ. Rungger and S. Sanvito, Phys. Rev. B 74, 024429 (2006).
- [43] S. L. Dudarev, G. A. Botton, S. Y. Savrasov, C. J. Humphreys, and A. P. Sutton, Phys. Rev. B 57, 1505 (1998).
- [44] V. I. Anisimov, J. Zaanen, and O. K. Andersen, Phys. Rev. B 44, 943 (1991).
- [45] V. P. Glazkov, D. P. Kozlenko, K. M. Podurets, B. N. Savenko, and V. A. Somenkov, Crystallogr. Reports 48, 54 (2003).
- [46] T. Suzuki and H. Ido, J. Phys. Soc. Japan 51, 3149 (1982).
- [47] A. Zunger, S.-H. Wei, L. G. Ferreira, and J. E. Bernard, Phys. Rev. Lett. 65, 353 (1990).
- [48] B. Alling, T. Marten, and I. A. Abrikosov, Phys. Rev. B 82, 184430 (2010).
- [49] P. Gorai, E. S. Toberer, and V. Stevanović, Phys. Chem. Chem. Phys. 18, 31777 (2016).
- [50] G. Trimarchi, Z. Wang, and A. Zunger, Phys. Rev. B 97, 035107 (2018).
- [51] J. Varignon, M. Bibes, and A. Zunger, Nat. Commun. 10, 1658 (2019).
- [52] D. J. Singh and M. H. Du, Phys. Rev. Lett. 100, 237003 (2008).
- [53] D. A. Papaconstantopoulos, M. J. Mehl, and M. D. Johannes, Phys. Rev. B 82, 054503 (2010).
- [54] R. Dronskowski and P. E. Bloechl, J. Phys. Chem. 97, 8617 (1993).
- [55] V. L. Deringer, A. L. Tchougréeff, and R. Dronskowski,

- J. Phys. Chem. A 115, 5461 (2011).
- [56] S. Maintz, V. L. Deringer, A. L. Tchougréeff, and R. Dronskowski, J. Comput. Chem. 34, 2557 (2013).
- [57] S. Maintz, V. L. Deringer, A. L. Tchougréeff, and R. Dron-
- skowski, J. Comput. Chem. 37, 1030 (2016).
- [58] S. Maintz, M. Esser, and R. Dronskowski, Acta Phys. Pol. B 47, 1165 (2016).

Supplemental Material for: Magnetostructural coupling from competing magnetic and chemical bonding effects

Joshua D. Bocarsly, Michelle Johannes, Stephen D. Wilson, and Ram Seshadri Materials Department and Materials Research Laboratory, University of California, Santa Barbara, California 93106, United States Center for Computational Materials Science, Naval Research Laboratory Washington, D.C. 20375, United States

(Dated: October 13, 2020)

I. Electronic structure calculation methods

A. Density functional theory calculations of ordered magnetic states

Electronic structure calculations were performed using density functional theory (DFT), as implemented in the Vienna Ab initio Simulation Package (VASP) [1] with projector augmented wave (PAW) pseudopotentials [2, 3] within the Perdew-Burke-Ernzerhof generalized gradient approximation (GGA) revised for solids (PBEsol) [4, 5]. A DFT+U approach was adopted, using the $U-J=U_{\rm eff}$ formalism of Dudarev [6], with the $U_{\rm eff}$ applied to the Mn d orbitals.

Once the appropriate $U_{\rm eff}=1.2\,{\rm eV}$ value was chosen (see below), calculations of the orthohexagonal unit cell [main text Fig. 1(b)] with varying amounts of Mn distortion and As distortion were performed. During the experimentally observed structural distortion from hexagonal to orthorhombic, the Mn atoms move principally along the c lattice direction, while the As atoms move along the a direction. Therefore, the parameters $\delta_{\rm Mn}=\Delta{\rm Mn}_z/c$ and $\delta_{\rm As}=\Delta{\rm As}_x/a$ were used to parameterize the distortion space. 900 calculations were performed on a 30 × 30 grid of $\delta_{\rm Mn}$ and $\delta_{\rm As}$ values ranging from –0.03 to 0.08. The Mn z parameter and As x parameter were kept fixed, while all of the other atomic coordinates and the unit cell were allowed to freely relax. Structural relaxations with an ionic convergence criterion of $1\times10^{-4}\,{\rm eV}$ were performed three times iteratively to ensure convergence, and then static calculations with an electronic convergence criterion of $1\times10^{-6}\,{\rm eV}$ were performed. Monkhorst-Pack k-point grids of $6\times8\times6$ were used, and all calculations were initialized with ferromagnetic moments of $3\,\mu_B$ on each Mn atom. Spin-orbit coupling was not included. In all calculations, the final configurations maintained Pnma symmetry and ferromagnetic ordering.

Similarly, linear potential surfaces only as a function of $\delta_{\rm Mn}$ were calculated, with the As z coordinate now being allowed to relax freely. For these calculations, an increased k-point grid of $6 \times 11 \times 5$ was used. The lattice parameters were initialized by linearly interpolating between the lattice parameters of the fully relaxed hexagonal structure ($\delta_{\rm Mn}$ = 0) and the local minimum energy orthorhombic structure, and then allowed to relax freely. These calculations were performed using both ferromagnetic and C-type antiferromagnetic moment initializations, and in all cases the magnetic ordering type stayed consistent with the initialization during relaxation. The results from each of these calculations were analyzed to obtain the crystal orbital Hamilton population (COHP) for nearby atoms and projected densities of states using the LOBSTER code [7–11]. The projected densities of states were calculated using a non-standard orientation of the d orbital basis set, as described in the main text and below. In order to do this, the static VASP calculations that fed into the LOBSTER calculations were performed with the MnAs structure rotated in 3d space such that correct Mn-Mn contacts were oriented along the cartesian z and x directions. pymatgen [12] was used to perform some of the cell manipulations and analysis, and VESTA [13] was used to visualize the structures and charge densities.

B. Simulation of paramagnetic state using special quasirandom structures

The paramagnetic state of MnAs was simulated using special quasi random structures (SQS) [14] obtained using mcsqs program [15] included within the ATAT package. A paramagnetic SQS is a supercell which is decorated with up and down moments on the Mn

atoms in such a way as to accurately reproduce the local spin-spin correlations expected in a random, dynamic paramagnet using just a single cell. A 96-atom SQS with supercell size $2 \times 3 \times 2$ of the the primitive orthorhombic cell was generated such that the 12 smallest pair correlations (radius up to 6 Å) and its first triplet correlation (radius 3.4 Å) match those of the random state. A full structural optimization was performed on this cell, starting with lattice parameters and atom positions from the lowest-energy AFM cell. The Mn atoms were each initialized with magnetic moments of positive or negative $3 \mu_B$ based on the constructed SQS, and symmetry was switched off such that the individual Mn and As atoms were each allowed to move in any direction and locally break the Pnma structural symmetry, and the cell was allowed to change shape arbitrarily. A Γ -centered k-point grid of $3 \times 3 \times 3$ was used. This structural optimization was performed several times iteratively, always resetting the initialized magnetic moments, until a final force convergence of $-0.005\,\mathrm{meV}\,\mathrm{\AA}^{-1}$ for all atoms was reached. The atoms all moved substantially away from their Pnma positions, and the quasirandom magnetic moments on each Mn atom remained stable with an overall cell moment of nearly zero. A static calculation with energy convergence of 1×10^{-6} eV was then performed, and the COHP was calculated. The resulting cell is shown in table S1.

Additionally, a 64-atom $2 \times 2 \times 2$ SQS was generated such that the 17 smallest pair correlations (radius up to 6.8 Å) match the random state. This cell was used to approximately obtain an energy surface of the random state as a function of $\delta_{\rm Mn}$ by performing selective dynamics structural relaxations on the SQS with fixed values of the Mn z parameters while all other atomic coordinates were allowed to fully relax. Structural optimizations were performed using a Γ -centered k-point grid of size $2 \times 4 \times 2$ and an energy convergence for the ionic loop of 0.001 eV. For each calculation in the energy surface, these optimizations were performed three times iteratively to ensure convergence.

TABLE S1. Relaxed lattice vectors, atom positions and local moments for the $2 \times 3 \times 2$ SQS

lattice vectors (Å):					
a	11.196	-0.018	0.003		
b	-0.017	10.715	0.020		
c	0.003	0.024	12.524		

atom	x	y	z	$\mu \; (\mu_B)$	atom	x	y	z	$\mu (\mu_B)$
Mn, up	0.9962	0.0796	0.1095	3.301	As	0.1466	0.0839	0.4570	-0.01
Mn, up	0.4982	0.4146	0.1113	3.141	As	0.6389	0.0796	0.4600	0.06
Mn, up	0.4992	0.7513	0.1053	3.161	As	0.1442	0.4135	0.4583	0.00
Mn, up	0.9980	0.4156	0.6073	3.105	As	0.6460	0.4192	0.4606	0.03
Mn, up	0.4986	0.7489	0.5998	3.271	As	0.1437	0.7508	0.4580	0.04
Mn, up	0.9973	0.7465	0.6048	3.222	As	0.6498	0.7493	0.4585	0.04
Mn, up	0.0030	0.2462	0.3921	3.283	As	0.1422	0.0849	0.9605	-0.09
Mn, up	0.5038	0.2524	0.4001	3.297	As	0.6447	0.0821	0.9578	0.08
Mn, up	0.0041	0.9208	0.3933	3.260	As	0.1445	0.4208	0.9609	-0.05
Mn, up	0.0029	0.2537	0.8928	3.301	As	0.6368	0.4211	0.9613	-0.05
Mn, up	0.5019	0.2452	0.8935	3.318	As	0.1395	0.7491	0.9618	-0.00
Mn, up	0.5025	0.5858	0.8884	3.061	As	0.6420	0.7511	0.9591	-0.04
Mn, up	0.2524	0.2546	0.8639	3.033	As	0.3553	0.2542	0.0427	-0.08
Mn, up	0.7513	0.5854	0.8574	3.219	As	0.8591	0.2487	0.0414	0.03
Mn, up	0.2538	0.5870	0.8593	3.245	As	0.3617	0.5834	0.0410	-0.14
Mn, up	0.2513	0.9112	0.8611	3.298	As	0.8563	0.5834	0.0372	0.05
Mn, up	0.2444	0.0801	0.6392	3.198	As	0.3585	0.9192	0.0418	-0.04
Mn, up	0.7457	0.4107	0.6436	3.231	As	0.8568	0.9118	0.0402	0.04
Mn, up	0.2450	0.4162	0.6418	3.160	As	0.3501	0.2498	0.5388	0.00
Mn, up	0.7475	0.7509	0.6439	3.012	As	0.8577	0.2515	0.5392	0.00
An, up	0.2467	0.0816	0.1462	3.382	As	0.3569	0.5806	0.5392	0.04
Иn, up	0.2484	0.4198	0.1463	3.231	As	0.8523	0.5823	0.5414	-0.03
Mn, up	0.7482	0.7471	0.1449	3.237	As	0.3588	0.9163	0.5394	0.05
Mn, up	0.7482 0.2495	0.7471	0.1449 0.1437	3.265	As	0.8554	0.9103	0.5384	0.00
An, down	0.4985	0.0898	0.1467	-3.280	As	0.3034 0.1047	0.2527	0.2085	-0.03
Mn, down	0.4983	0.4178	0.1050 0.1054	-3.186	As	0.6116	0.2527 0.2501	0.2003	0.07
Mn, down	0.9979	0.7464	0.1094 0.1091	-3.196	As	0.1093	0.2301 0.5820	0.2100 0.2103	0.07
	0.4942	0.0835	0.6105	-3.190 -3.287	As	0.6052	0.5825	0.2103	0.00
An, down									
An, down	0.9971 0.4950	0.0828	0.6057	-3.420	As	0.1063	0.9125	0.2105	-0.03
An, down		0.4125	0.6059	-3.368	As	0.6081	0.9172	0.2088	0.05
In, down	0.0027	0.5816	0.3955	-3.270	As	0.1106	0.2485	0.7128	-0.10
An, down	0.5053	0.5876	0.3930	-3.161	As	0.6048	0.2480	0.7118	0.03
An, down	0.5041	0.9125	0.3905	-3.192	As	0.1048	0.5796	0.7099	-0.04
An, down	0.0030	0.5845	0.8896	-3.148	As	0.6090	0.5822	0.7086	-0.10
Mn, down	0.0021	0.9204	0.8911	-3.275	As	0.1036	0.9134	0.7106	0.00
In, down	0.5008	0.9206	0.8909	-3.290	As	0.6089	0.9159	0.7093	0.03
In, down	0.7518	0.2598	0.8599	-3.349	As	0.3991	0.0873	0.2909	0.0
In, down	0.7533	0.9138	0.8571	-3.148	As	0.8862	0.0820	0.2907	0.01
Mn, down	0.7535	0.2487	0.3602	-3.297	As	0.3970	0.4183	0.2941	0.01
In, down	0.2546	0.2516	0.3489	-3.195	As	0.8932	0.4166	0.2902	0.10
In, down	0.7537	0.5840	0.3563	-3.071	As	0.3952	0.7493	0.2902	0.04
Mn, down	0.2534	0.5829	0.3588	-3.123	As	0.8955	0.7512	0.2919	0.05
Mn, down	0.7530	0.9136	0.3564	-3.105	As	0.3819	0.0852	0.7907	-0.04
Mn, down	0.2556	0.9171	0.3539	-3.246	As	0.8866	0.0871	0.7904	0.08
Mn, down	0.7464	0.0834	0.6383	-3.246	As	0.3918	0.4180	0.7912	-0.10
Mn, down	0.2460	0.7469	0.6451	-3.370	As	0.8943	0.4201	0.7882	-0.05
Mn, down	0.7468	0.0821	0.1390	-3.162	As	0.3962	0.7527	0.7872	-0.03
Mn, down	0.7487	0.4207	0.1422	-3.277	As	0.8950	0.7487	0.7879	-0.01

II. Choice of U_{eff} parameter

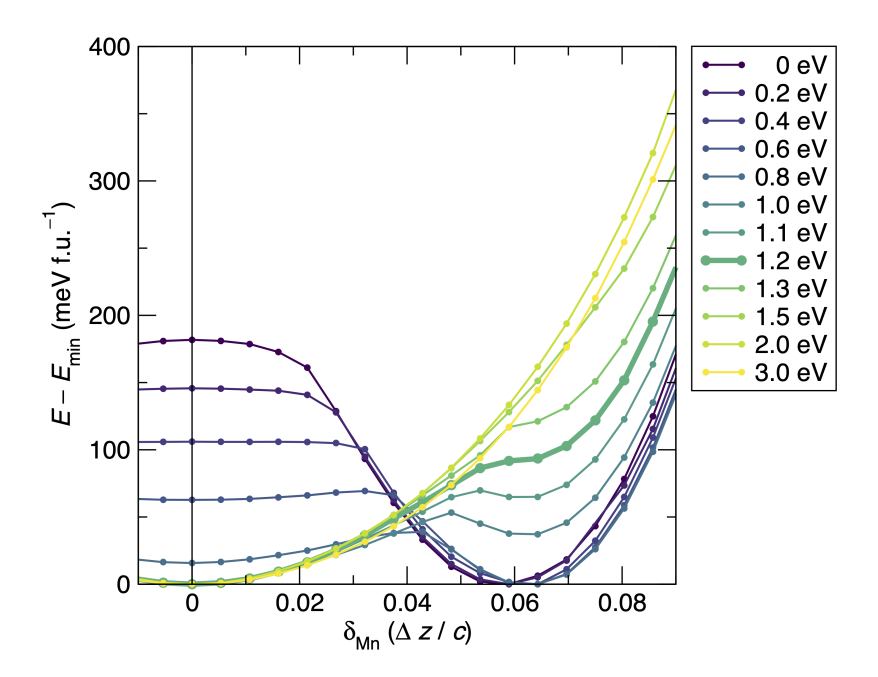


FIG. S1. Dependence of the MnAs distortion energy landscape on the $U_{\rm eff}=U-J$ parameter added to the Mn d-orbitals. With $U_{\rm eff}=0$, the distorted orthorhombic low-moment structure is erroneously lower in energy than the true (experimentally observed) hexagonal ground state $(\delta_{\rm Mn}=0)$. Upon adding the U correction, the hexagonal state is stabilized relative to the orthorhombic state and becomes lower in energy for $U_{\rm eff}=1.0\,{\rm eV}$ and above. The curve for the U value selected for use in our study ($U_{\rm eff}=1.2\,{\rm eV}$) is shown in bold. It should be noted that the chosen value of $U_{\rm eff}$ is dependent on the details of DFT calculations. For example, when we attempted to use the standard PBE GGA instead of PBEsol, the qualitative behavior of the energy curves remained the same but the optimal $U_{\rm eff}$ was found to be 0.5 eV.

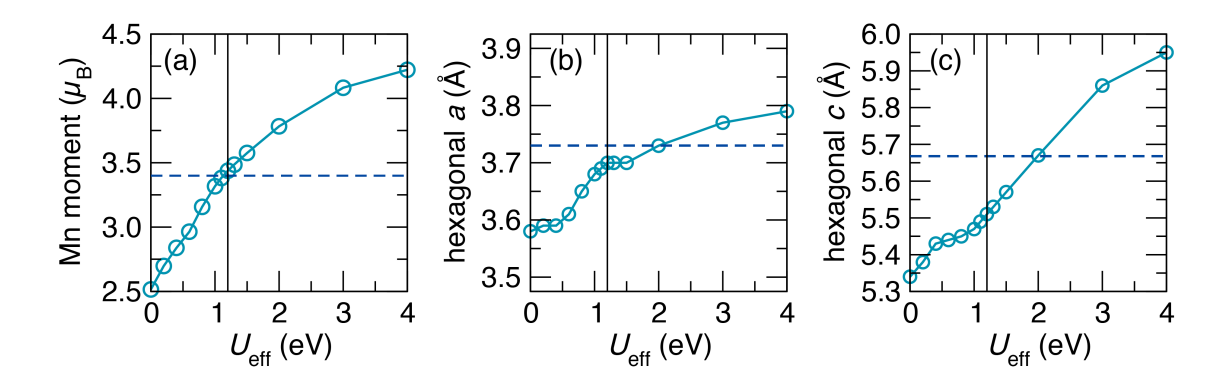


FIG. S2. Dependence of (a) the local Mn moment and (b-c) fully relaxed lattice parameters for hexagonal MnAs on $U_{\rm eff}$. For each parameter, the experimental value [16, 17] is shown as a horizontal line. $U_{\rm eff}=0$ gives very large deviations from the experimental situation, while a $U_{\rm eff}$ value of 1.2 eV correctly models the moment and underestimates the hexagonal a and c parameters by just 0.8% and 2.7%, respectively.

III. Calculations using the PBE functional

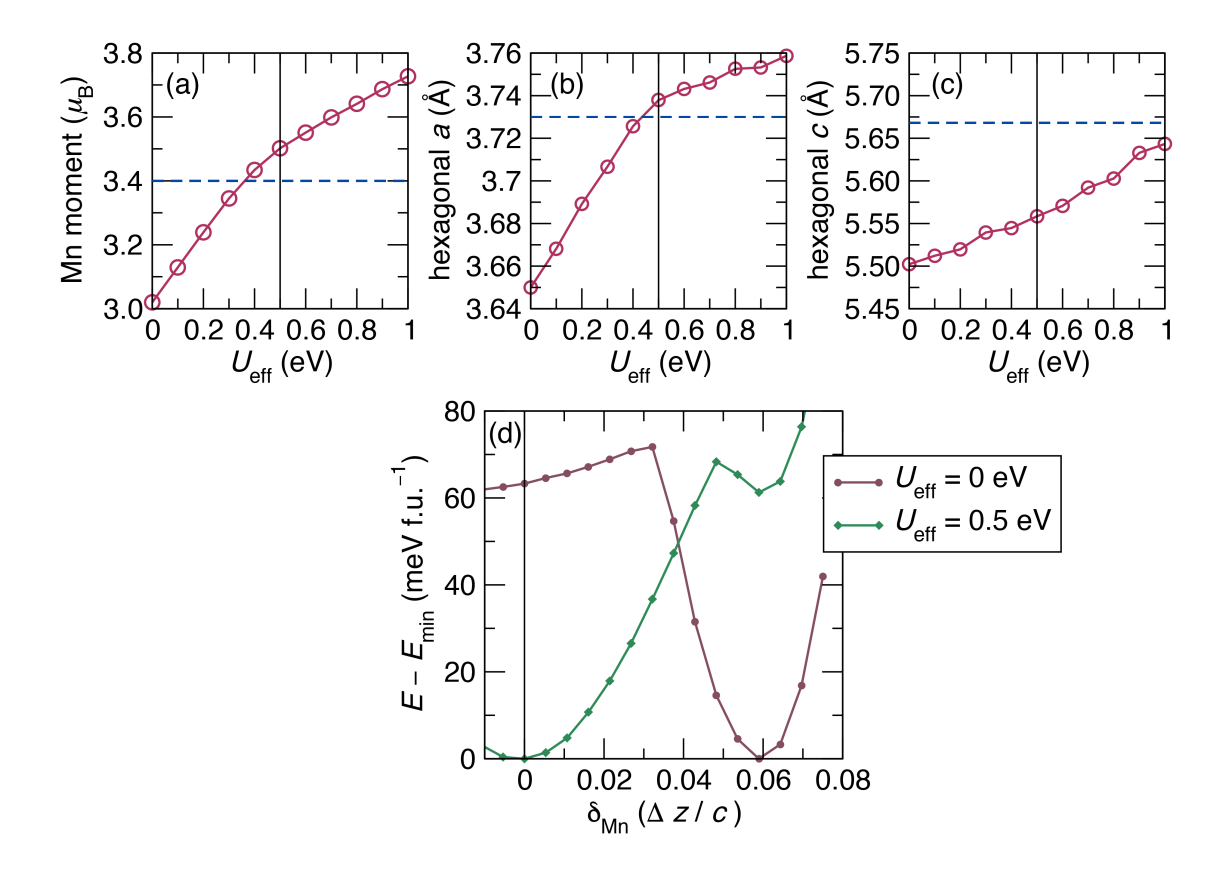


FIG. S3. Calculations of MnAs performed using the standard PBE functional, instead of PBEsol. Similar results are found: for $U_{\rm eff}=0$, the Mn local moment (a) and lattice parameters (b-c) are all smaller than experiment, and the low-moment orthorhombic state around $\delta_{\rm Mn}=0.06$ is erroneously lower in energy than the hexagonal state (d). The application of a small $U_{\rm eff}=0.5\,{\rm eV}$ improves the agreement with experiment, giving very similar results to PBEsol with $U_{\rm eff}=1.2\,{\rm eV}$.

IV. Comparison of calculated structures and magnetic moments with experiment

TABLE S2. Comparison of experimental lattice parameters, structural parameters, and magnetic moments with the results of the various DFT calculations. In each case, the calculation best matching the experimental parameters is bolded.

Hexagonal, FM state (ground state)

	a (Å)	c (Å)	$\operatorname{Mn} \mu (\mu_B)$
experiment, 4 K [18, 19]	3.73	5.668	3.4
$FM, U_{eff} = 0 eV$	$3.58 \; (-4.1\%)$	$5.34\ (-5.9\%)$	2.5
$\mathrm{FM},U_{\mathrm{eff}}{=}1.2\mathrm{eV}$	$3.70\ (-0.9\%)$	5.51 (-2.7%)	3.4

Orthorhombic, FM state under pressure

	a (Å)	b (Å)	c (Å)	$\delta_{ m Mn}$	$\delta_{ m As}$	$\operatorname{Mn} \mu (\mu_B)$
expt. 38 kbar 295 K [20]	5.495	3.414	6.103	0.050	0.050	2.3
low-moment FM	5.60 (1.9%)	$3.39\ (-0.8\%)$	$5.97\ (-2.1\%)$	0.060	0.053	2.4

Orthorhombic, PM state at ambient pressure

	a (Å)	b (Å)	c (Å)	$\delta_{ m Mn}$	$\delta_{ m As}$	Mn local μ
						(μ_B)
expt. 318 K [16, 21]	5.72	3.676	6.379	0.027(2)	0.025(2)	3.1(2)
low-moment FM	$5.40\ (-5.6\%)$	$3.36 \ (-8.6\%)$	$5.96\ (-6.6\%)$	0.060	0.053	2.4
AFM	$5.56\ (-2.7\%)$	$3.52\ (-4.3\%)$	$6.16\ (-3.5\%)$	0.047	0.050	3.0
SQS	$5.60\ (-2.1\%)$	$3.57\ (-2.8\ \%)$	6.26 (-1.8 %)	0.035	0.036	3.2

V. 2-D maps of moment and volume for ferromagnetic MnAs

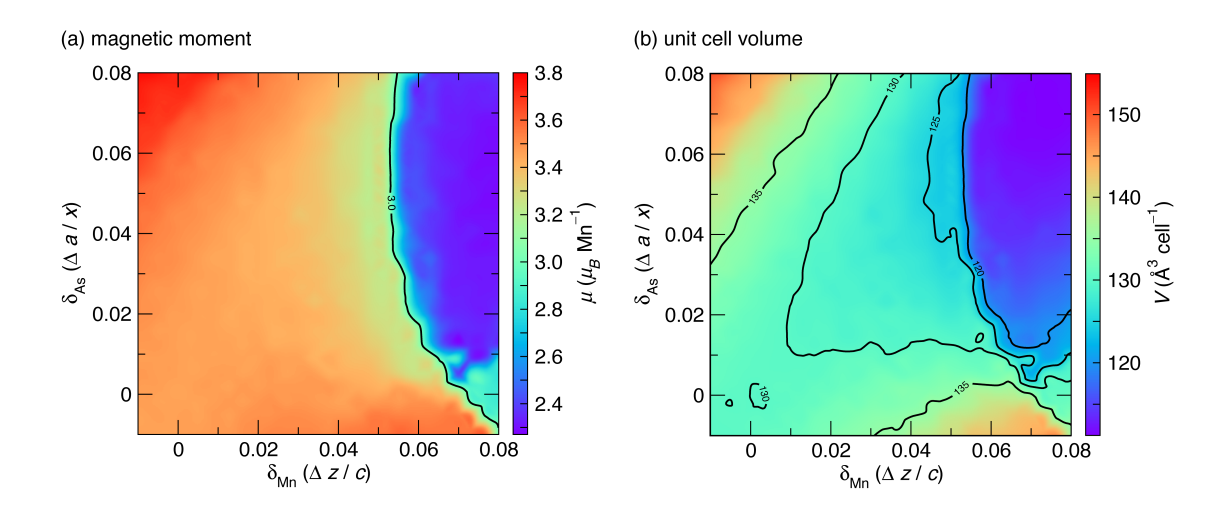


FIG. S4. Maps of magnetic moment and unit cell volume as a function of Mn and As distortion magnitudes, from the calculations shown in main text Fig. 2(a).

VI. Partial DOS for individual Mn d orbitals using conventional octahedral basis

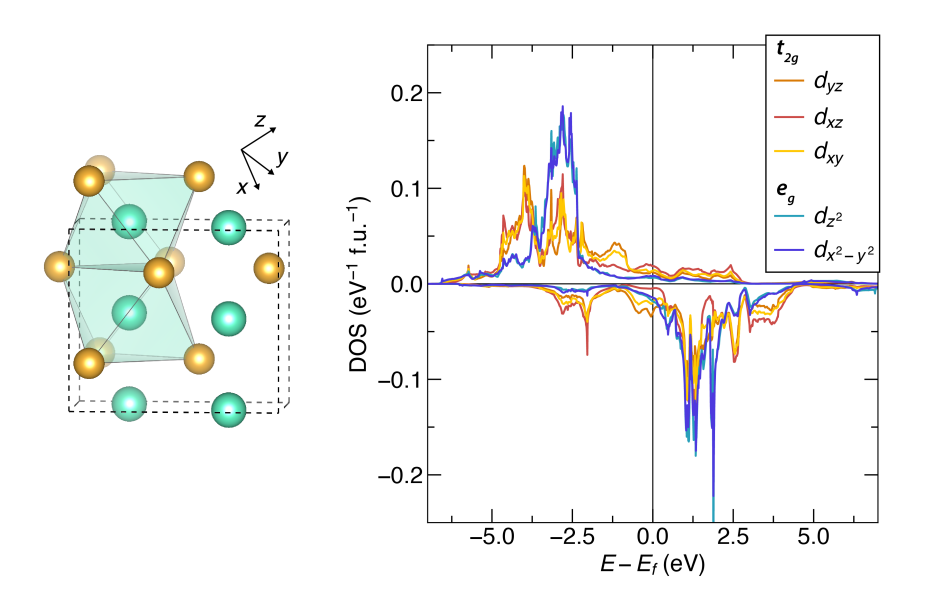


FIG. S5. Hexagonal FM state partial densities of states (pDOS) for the Mn d orbitals in the conventional octahedral projection scheme. While the t_{2g} and e_g sets of orbitals are each approximately degenerate, both sets show multiple peaks and the overall electronic structure does not exhibit the traditional splitting between localized t_{2g} and e_g manifolds. For this reason, we found this projection scheme to be of limited utility in studying the behavior of MnAs and moved to a projection scheme oriented around the Mn-Mn contacts (below).

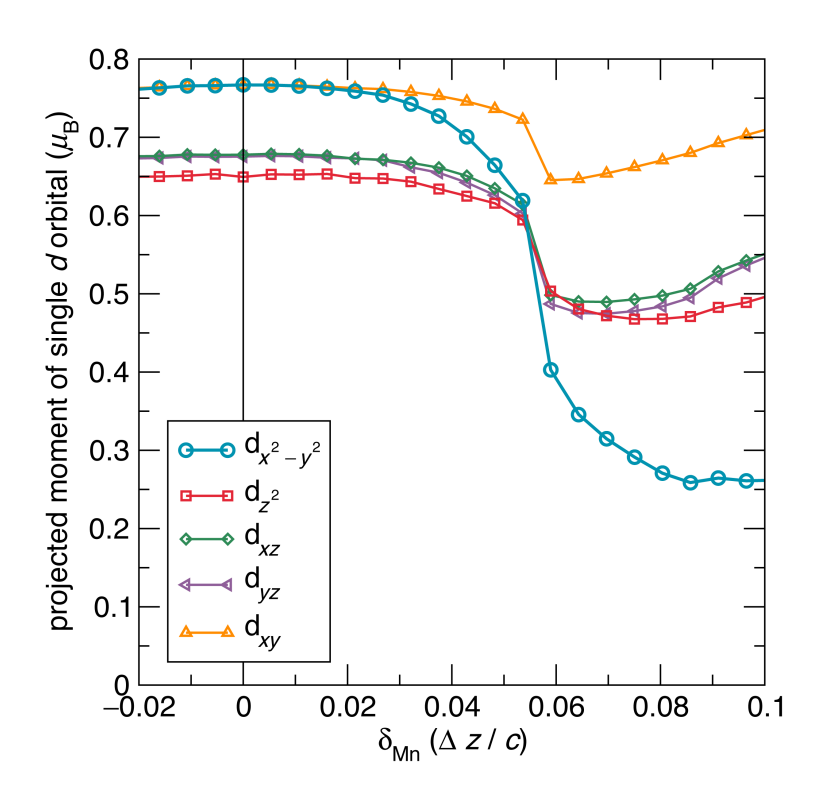


FIG. S6. Changes in the moment of each Mn d orbital as a function of Mn distortion ($\delta_{\rm Mn}$) for the ferromagnetic case. The $d_{x^2-y^2}$, which points one of its lobes along the Mn-Mn zigzag contact that is activated by the Mn distortion mode, experiences a drastic reduction in moment of 55% between the hexagonal and low-moment orthorhombic structure. On the other hand, the changes in the other orbitals are much smaller, emphasizing the importance of the $d_{x^2-y^2}$ orbital to the structural transitions in MnAs.

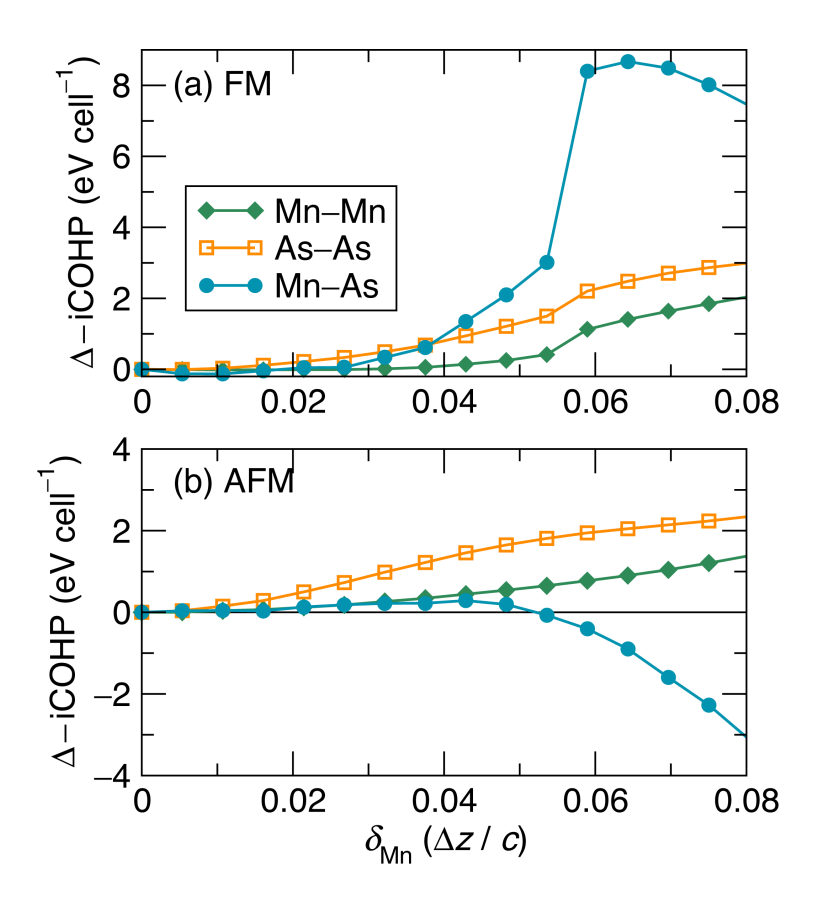


FIG. S7. Changes in MnAs bond strengths (estimated using the per cell change in negative integrated crystal orbital Hamilton population, Δ –iCOHP) as a function of $\delta_{\rm Mn}$ for (a) the ferromagnetic spin arrangement and (b) C-type antiferromagnetic spin arrangement. The largest change in –iCOHP for a single bond is observed in the Mn-Mn zigzag contact, as shown in the main text Fig. 4. However, since there are many more Mn-As and As-As contacts within the unit cell, the total changes in Mn-As and As-As –iCOHPs per cell are generally larger than the Mn-Mn contribution. From these calculations, it can be see that the overall bonding is optimized around $\delta=0.06$ for the FM case, and $\delta=0.05$ for the AFM case.

VII. Additional bond-lengths and -iCOHPs in the relaxed SQS cell

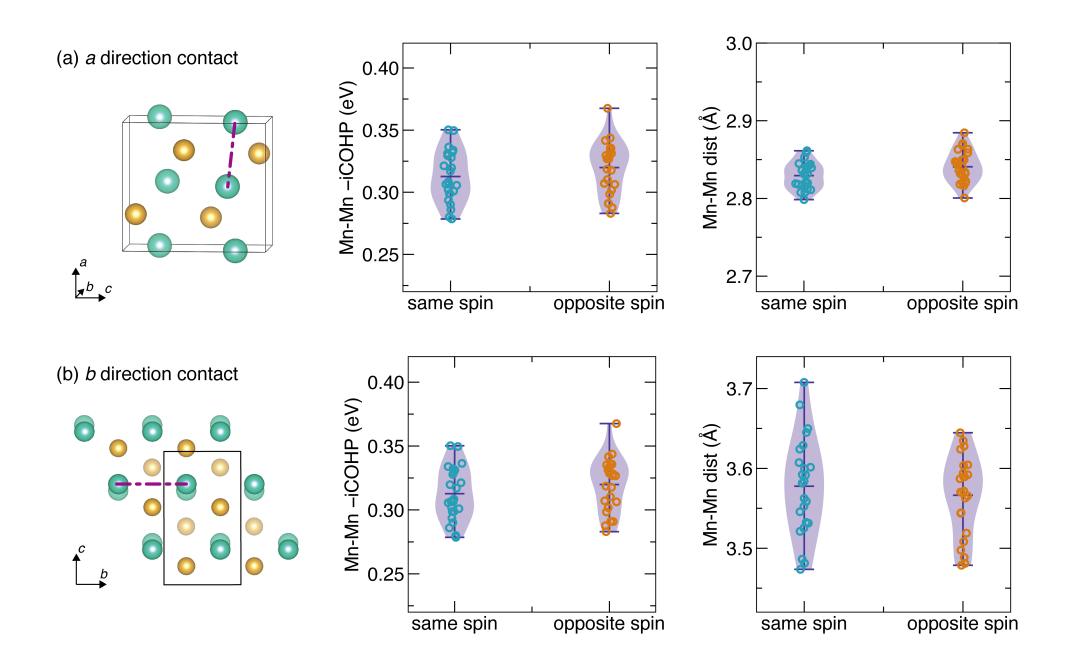


FIG. S8. Distributions of bond distances and –iCOHPs extracted from the relaxed SQS cell, for (a) the out-of-plane Mn-Mn contacts and (b) the Mn-Mn contacts along the orthorhombic b direction. These data are analogous to the data shown for the Mn-Mn zigzag contact in the main text Fig. 5. Unlike the zigzag contact, the two contacts shown here do not exhibit a dependence of bond length or –iCOHP on the spin correlation. This observation highlights that the competition-driven magnetostructural coupling is only active in a single Mn d orbital, the $d_{x^2-y^2}$ orbital discussed in the main text.

[1] G. Kresse and J. Furthmüller, Efficient iterative schemes for *ab initio* total-energy calculations using a plane-wave basis set, Phys. Rev. B **54**, 11169 (1996).

^[2] P. E. Blöchl, Projector augmented-wave method, Phys. Rev. B 50, 17953 (1994).

^[3] G. Kresse and D. Joubert, From ultrasoft pseudopotentials to the projector augmented-wave method, Phys. Rev. B **59**, 1758 (1999).

^[4] J. P. Perdew, K. Burke, and M. Ernzerhof, Generalized gradient approximation made simple, Phys. Rev. Lett. **77**, 3865 (1996).

^[5] J. P. Perdew, A. Ruzsinszky, G. I. Csonka, O. A. Vydrov, G. E. Scuseria, L. A. Constantin, X. Zhou, and K. Burke, Restoring the density-gradient expansion for exchange in solids and surfaces, Phys. Rev. Lett. 100, 136406 (2008).

^[6] S. L. Dudarev, S. Y. Savrasov, C. J. Humphreys, and A. P. Sutton, Electron-energy-loss spectra and the structural stability of nickel oxide: An LSDA+U study, Phys. Rev. B 57, 1505 (1998).

^[7] R. Dronskowski and P. E. Bloechl, Crystal orbital Hamilton populations (COHP): energy-

- resolved visualization of chemical bonding in solids based on density-functional calculations, J. Phys. Chem. **97**, 8617 (1993).
- [8] V. L. Deringer, A. L. Tchougréeff, and R. Dronskowski, Crystal Orbital Hamilton Population (COHP) analysis as projected from plane-wave basis sets, J. Phys. Chem. A 115, 5461 (2011).
- [9] S. Maintz, V. L. Deringer, A. L. Tchougréeff, and R. Dronskowski, Analytic projection from plane-wave and PAW wavefunctions and application to chemical-bonding analysis in solids, J. Comput. Chem. 34, 2557 (2013).
- [10] S. Maintz, V. L. Deringer, A. L. Tchougréeff, and R. Dronskowski, LOBSTER: A tool to extract chemical bonding from plane-wave based DFT, J. Comput. Chem. **37**, 1030 (2016).
- [11] S. Maintz, M. Esser, and R. Dronskowski, Efficient rotation of local basis functions using real spherical harmonics, Acta Phys. Pol. B 47, 1165 (2016).
- [12] S. P. Ong, W. D. Richards, A. Jain, G. Hautier, M. Kocher, S. Cholia, D. Gunter, V. L. Chevrier, K. A. Persson, and G. Ceder, Python Materials Genomics (pymatgen): A robust, open-source python library for materials analysis, Comput. Mater. Sci. 68, 314 (2013).
- [13] K. Momma and F. Izumi, VESTA 3 for three-dimensional visualization of crystal, volumetric and morphology data, J. Appl. Crystallogr. 44, 1272 (2011).
- [14] A. Zunger, S.-H. Wei, L. G. Ferreira, and J. E. Bernard, Special quasirandom structures, Phys. Rev. Lett. 65, 353 (1990).
- [15] A. van de Walle, P. Tiwary, M. de Jong, D. Olmsted, M. Asta, A. Dick, D. Shin, Y. Wang, L.-Q. Chen, and Z.-K. Liu, Efficient stochastic generation of special quasirandom structures, Calphad 42, 13 (2013).
- [16] R. H. Wilson and J. S. Kasper, The crystal structure of MnAs above 40°C, Acta Crystallogr. 17, 95 (1964).
- [17] N. Menyuk, J. A. Kafalas, K. Dwight, and J. B. Goodenough, Effects of pressure on the magnetic properties of MnAs, Phys. Rev. 177, 942 (1969).
- [18] A. Zieba, K. Selte, A. Kjekshus, A. F. Andresen, O. Smidsrød, C.-O. Pontchour, P. Phavanantha, S. Pramatus, B. N. Cyvin, and S. J. Cyvin, Phase transitions in MnAs, Acta Chem. Scand. **32a**, 173 (1978).
- [19] C. Guillaud, Les points de transformation des composés définis MnAs, MnBi en relation avec un mécanisme probable d'antiferromagnétisme, J. Phys. le Radium 12, 223 (1951).
- [20] V. P. Glazkov, D. P. Kozlenko, K. M. Podurets, B. N. Savenko, and V. A. Somenkov, Neutron diffraction investigation of the atomic and magnetic structures of MnAs at high pressures, Crystallogr. Reports 48, 54 (2003).
- [21] L. H. Schwartz, E. L. Hall, and G. P. Felcher, Magnetic structure of MnAs and MnAs_{0.92}P_{0.08}, J. Appl. Phys. 42, 1621 (1971).